J Solid State Electrochem (2006) 10: 604–616
DOI 10.1007/s10008-006-0139-6

ORIGINAL PAPER

A. Thursfield · I. S. Metcalfe

Methane oxidation in a mixed ionic–electronic conducting ceramic hollow fibre reactor module

Received: 15 December 2005 / Accepted: 20 December 2005 / Published online: 30 March 2006

Abstract A reactor module, consisting of six gas-tight hollow fibre membranes made of the mixed ionic–electronic conducting perovskite, $La_{0.6}Sr_{0.4}Co_{0.2}Fe_{0.8}O_{3-\delta}$ has been tested for oxygen permeation and stability during methane oxidation in the temperature range of 540 to 960°C. Rigorous leak testing was undertaken and it was demonstrated that the module could be adequately sealed. Oxygen permeation fluxes were similar to those reported by previous workers. At higher temperatures of operation, it appeared that mass transfer limited the oxygen flux, as this flux was dependent upon the flow rates on either side of the membrane. In this way, reactant flow rates could be used to manipulate the transmembrane oxygen flux. It was found that the product distribution on the methane side was dependent upon this flux, with carbon monoxide and hydrogen production being favoured at low fluxes and carbon dioxide and water production being favoured at higher fluxes. Furthermore, at low oxygen flow rates, periodic increases in the transmembrane oxygen flux were observed. The cause of this behaviour is unclear but may be as a result of phase/stoichiometric changes associated with the membrane material.

Keywords Perovskite · $La_{0.6}Sr_{0.4}Co_{0.2}Fe_{0.8}O_{3-\delta}$ · Mixed conductor · Hollow fibre · Oxygen permeation · Methane oxidation · Leak test

Introduction

The continuous emission of carbon dioxide into the atmosphere by developed nations and the ever increasing contribution from the developing world have resulted in increased concerns about the acceleration of global warming and resultant climate change. The projected carbon dioxide release into the atmosphere by 2008 to 2012 is estimated to be around 2,600 million metric tonnes [1]. The energy sector is a major contributor worldwide, combusting fossil fuels such as methane in conventional turbine power generators and emitting diluted carbon dioxide as a waste product in the flue gas. Whilst carbon dioxide is taken up by natural planetary sinks, such as the ocean (which has the largest capacity), soil, vegetation and stable carbonate formation with minerals, this natural process is slow.

One of the many strategies being investigated to reduce carbon dioxide emissions focuses on capturing it from the flue gas of conventional power stations. This idea has been applied using, e.g., monoethanolamine as an absorbent to capture the carbon dioxide. Whilst this process is proven, it suffers from problems such as solvent degradation, corrosion, large equipment volumes and high regeneration energy requirements. An alternative approach is to integrate a high temperature ceramic membrane separation system into existing power plants. The advanced zero emission power plant exploits a class of mixed ionic and electronic (MIEC) conducting mixed metal oxides in membrane form that are based on the well-known perovskite metal oxide of general formula ABO_3, with A representing a group II or lanthanide element and B a transition metal. At high temperature and under an oxygen activity difference, such a membrane can theoretically supply pure oxygen to the hydrocarbon fuel side, allowing the use of air as a freely available supply of oxygen whilst excluding nitrogen and other gases [2] (see Fig. 1).

The oxygen is disassociated on the membrane surface and incorporated as oxygen ions, O^{2-}, that migrate through the crystal lattice via oxygen vacancy defect sites. Slow surface kinetics, between the adsorbed oxygen and the membrane surface, and large membrane thicknesses are hindrances to transmembrane oxygen transport. On the fuel side, oxygen ions react with the hydrocarbon to produce carbon oxides, hydrogen and water. Under conditions of complete oxidation, carbon dioxide and water are produced and carbon dioxide can easily be recovered (the use of the

A. Thursfield · I. S. Metcalfe (✉)
School of Chemical Engineering and Advanced Materials,
University of Newcastle upon Tyne,
Newcastle upon Tyne, NE1 7RU, UK
e-mail: I.Metcalfe@newcastle.ac.uk
Tel.: +44-191-2225279
Fax: +44-191-2225292

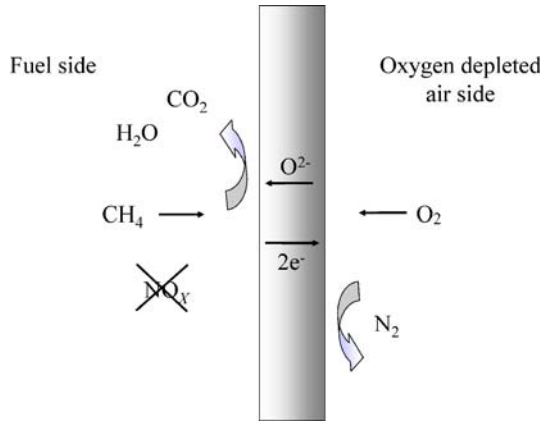

Fig. 1 Principle of high temperature operation of a MIEC ceramic membrane exclusively allowing oxygen to be transported under a chemical potential difference through to the hydrocarbon fuel side to facilitate oxidation reactions

membrane avoids the difficult nitrogen–carbon dioxide separation).

The perovskite metal oxides have attracted much attention over the years as the readily modifiable crystal structure has lead to tuning of physicochemical properties by selective doping in of metal cations at the A and B sites [3–7]. The studies in which MIEC perovskites are used for oxygen permeation and chemical synthesis in catalytic membrane reactors is ever increasing with particular attention paid to syngas (hydrogen and carbon monoxide) production from methane [8]. Stability of the crystal structure is a prominent issue, as exposure to large chemical potential gradients that are established when such a membrane separates oxygen and a hydrocarbon fuel can cause degradation of the membrane and, subsequently, a decline in performance with time. This degradation may arise from processes such as segregation of constituent metal cations, formation of carbonates, formation of other related crystalline phases, such as brownmillerite, and lattice expansion from the reduction of transition metal cations. The $La_{1-x}Sr_xCo_{1-y}Fe_yO_{3-\delta}$ [9] perovskite family has been studied for a number of years, and their electronic and oxide anion conductivity has been thoroughly investigated [10]. One of the most studied members of this family is the particularly robust $La_{0.6}Sr_{0.4}Co_{0.2}Fe_{0.8}O_{3-\delta}$ hereafter abbreviated to LSCF6428. The oxygen permeation characteristics of this member have been studied in detail [11, 12], using mostly disc membranes of typical dimensions 1-mm thick and having a surface area of 1 cm^2; occasionally tubular membranes of similar thickness and length of a few centimetres have also been employed [13]. Recent advances in membrane fabrication methods have allowed the fabrication of gas-tight, thin hollow fibres by a phase inversion method [14, 15]. The hollow fibres provide a high-membrane surface area per unit volume of reactor compared to the disc and tubular forms. They are formed from ceramic powder, which is mixed with a polymer binder and solvent; the resultant dope is extruded under pressure through a spinneret. This gives membranes a constant circular cross-section, with diameters typically around 1 to 2 mm and wall thicknesses in the range 0.2 to 0.3 mm and lengths, depending on furnace length, of the order of 20 to 30 cm after sintering. The submillimetre wall thicknesses should allow for greater oxygen permeation and possibly allow the use of lower temperatures to obtain the equivalent flux obtained from a typical disc or tube membrane. Ceramic hollow fibres are a relatively recent development, but work is underway to produce more sophisticated multi-layered ceramic hollow fibres [16] and modification of the cross-section shape by using spinnerets of shapes other than a simple circle [17].

In this contribution, we report on the performance of a MIEC LSCF6428 hollow fibre reactor module with respect to oxygen permeation over the temperature range of 540 to 960°C. Following this study, the module's performance was tested for its suitability for methane oxidation. Throughout these studies, the sealing of the module was monitored, as well as the gas tightness of the hollow fibre membranes under operating conditions.

Experimental

Commercial LSCF6428 (Praxair) was used to produce the dense hollow fibre membranes by the phase inversion technique. This method and the membrane gas-tightness testing apparatus are described elsewhere [14]. A spinneret, with an outer diameter of 3 mm and inner diameter of 1.2 mm, was used to produce long lengths of the green, followed by sintering at 1,280°C for 4 h. Phase purity was

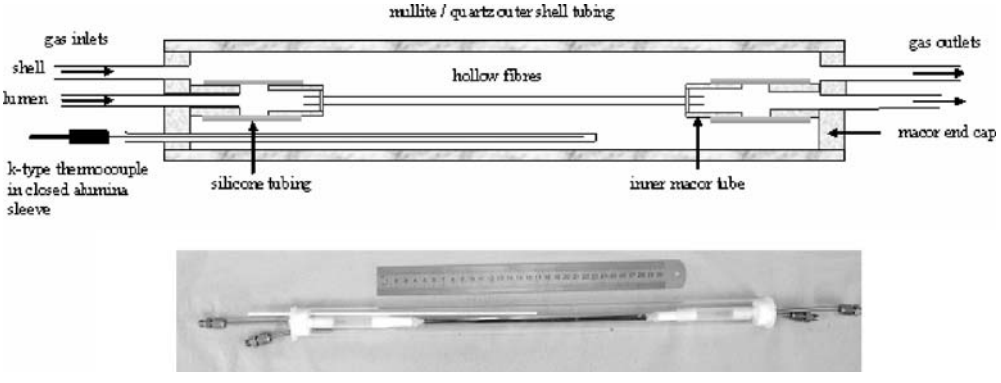

Fig. 2 Diagram of the hollow fibre module used for the oxygen permeation and methane combustion studies. A photo image of a typical module is also shown with a 30 cm rule for scale

ascertained by powder X-ray diffraction (XRD) using a Philips 3040/60. A Quanta 200 and 30XL (FEI) were used to perform scanning electron microscopy (SEM) for microstructure characterisation. The hollow fibres employed in this work had a nominal length of 25 cm, outer diameter of 1.5 mm and inner diameter 1 mm.

The membrane performance apparatus employed consisted of: gas supply, gas flow control and the hollow fibre reactor module with furnace and gas analysis instrumentation. All experiments were performed at 1 atm on both sides of the membrane. The gas supplies to the reactor module in all experiments were controlled by Chell Hastings mass flow controllers calibrated for 100% helium and ranged from 0 to 90 ml min^{-1}. All gas flows are quoted at standard temperature and pressure (STP).

Reactor module assembly and furnace system

A diagram of the hollow fibre reactor module is given in Fig. 2 along with a photo image of a typical module.

The shell material is either made of mullite or quartz and measures 40 cm in length with an internal diameter of 2.6 cm and external diameter of 3.0 cm. An inert alumina sleeve runs through the module, close to the hollow fibres and houses a K-type thermocouple accurate to within ±0.1°C, which could be moved along the length of the module. The two pairs of gas inlets/outlets are made of stainless steel with 1/8 in. Swagelok compression fittings. These are housed in MACOR end caps (Precision Ceramics, UK) that fit closely to the inner wall of the shell tubing. The hollow fibres are placed in the module using a pair of MACOR tubes; each tube is closed at one end and has holes drilled through to accommodate the ends of the hollow fibres. The other end of the MACOR tube is completely open. The open end of the tubes is attached to the lumen side gas inlet/outlet by a length of flexible silicone tubing rated to 238°C. The silicone tubing allowed flexibility to accommodate the thermal expansion of the hollow fibres. The sealing was achieved by using a combination of water-based glass–ceramic sealant (Fortifix, UK) for the hollow fibres and silicone sealant for the end caps, gas inlet–outlets and thermocouple sleeve. The integrity of the seals is maintained by taking advantage of the length of the hollow fibres in conjunction with the use of a small furnace. Six hollow fibres were used. Gas flow through the hollow fibres is referred to as being on the "lumen side", and gas flow outside of the hollow fibres is referred to as being on the "shell side". Permeation refers only to the activated solid-state oxygen transport through the hollow fibres and does not include any contribution from leakage, which is separately determined by procedures described later.

The custom-made furnace (Vecstar Furnaces, UK) was equipped with an eight-segment Eurotherm controller and had a total length of 15 cm. The heated zone was 13 cm in length, with a central linear heating zone of 5 cm and a bore diameter of 3.7 cm. The central zone had a drop of 30°C from its centre point over the operating temperature range of concern. It was assumed that the furnace gave a symmetrical temperature profile. Temperature profiles at the interior of the reactor module for a number of furnace temperature settings and under one set of flow conditions are presented in Fig. 3.

The thermocouple tip was initially positioned at the centre of the hollow fibres and was moved out in 0.5- or 1-cm steps from the centre of the hollow fibre module to a few centimetres outside of the furnace. The small furnace dimensions ensured that the sealing points were situated approximately 3 cm outside of the furnace and benefited from the cooling effect of the atmosphere. The highest temperature recorded at the hollow fibre-MACOR tube sealing point was 170°C at a furnace setting of 1,000°C, which gave 958°C measured at the centre of the module

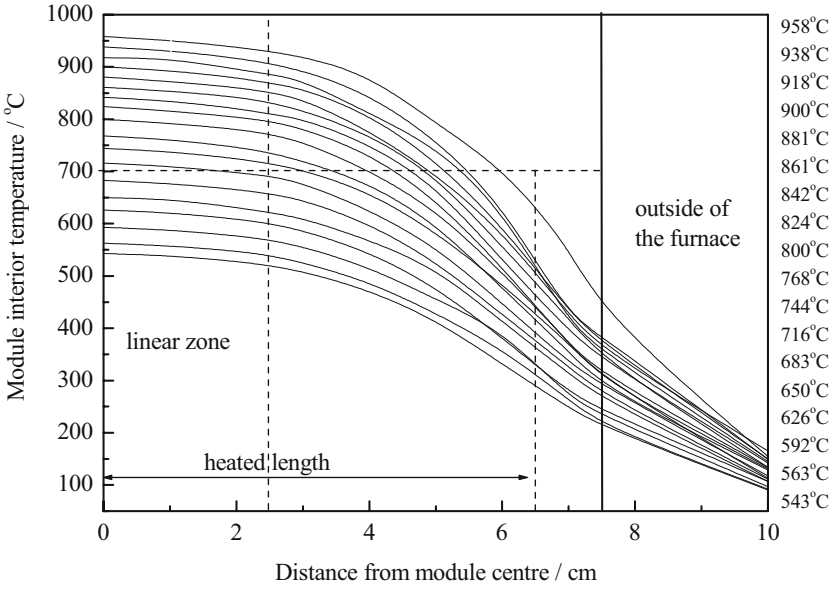

Fig. 3 Internal temperature profiles of the reactor module obtained for furnace settings from 565 to 1,000°C obtained under a flow of 21% oxygen, balance nitrogen, at 50 ml min^{-1} on the shell side and a pure helium flow at 50 ml min^{-1} on the lumen side. Listed on the *right hand side* are the actual temperatures measured at the centre of the module. The temperature profile also shows the most severe temperature at the point of sealing of the hollow fibres at 10 cm. Marked on the graph for reference are the *central linear temperature zone* and the *total heated length*, and the *heavy vertical line* indicates the total length of the furnace

close to the hollow fibres (when reporting operating temperatures, we refer to the temperature at the centre of the module). A heating or cooling rate of 3°C min^{-1} was used throughout this investigation. When using discs or small tubes, where such membranes are smaller than the furnace hot zone length, it is easy to achieve isothermal operation. In this study, such an assumption cannot be made as evidenced in Fig. 3. The experimental setup addresses the problem of sealing but produces the problem of a varying oxygen flux along the length of the hollow fibres due to the temperature profile of the furnace. With increasing temperatures, more and more of the hollow fibre membrane becomes activated for permeation. The system's active surface area is therefore not fixed, as from one operating temperature to a significantly different operating temperature, the active surface areas will be different, resulting in incomparable fluxes. However, the superficial membrane surface area S_A provided by the module can be approximated by

$$S_A = \frac{2\pi(r_o - r_i)}{\ln(r_o/r_i)} nl \quad (1)$$

where r_o and r_i are the outer and inner radius, respectively, of a typical hollow fibre, n is the number of hollow fibres, and l is the activated working length, which is temperature-dependent (Fig. 3). The radii r_o and r_i were typically 0.07 and 0.05 cm, respectively, although this is an approximation because of irregular wall thicknesses. Assuming that only the central linear heating zone of the furnace is used (l=5 cm) gives an active membrane area of ca 10 cm^{-2} provided by the six hollow fibres.

Gas analysis

Molar inlet and outlet compositions were obtained by gas chromatography (GC) using a Varian CP-3800 with series-bypass capability. Molecular sieve 5A and Haysep Q columns were used for gas component separation in conjunction with a thermal conductivity detector and helium carrier gas flow of 30 ml min^{-1}. For the oxygen permeation experiments and leak testing, two calibration gas standards were used: 0.5% oxygen and 0.5% nitrogen (balance helium) and 4% oxygen and 4% nitrogen (balance helium). The mole fractions in both mixtures were accurate to ±5% of the nominal mole fraction. For the methane oxidation experiments, GC calibration was performed using a single gas standard mixture consisting of 2% hydrogen, 0.5% oxygen, 2% nitrogen, 2% methane, 2% carbon monoxide, 2% carbon dioxide, 2% ethene and 2% ethane (mole fractions with ±2% accuracy).

All composition measurements were made from three to five times to test repeatability. Based upon the uncertainty in these measurements and the uncertainty in the composition of the calibration gases, error estimates were made for the mole fractions determined. Propagation of these errors, combined with allowing for the presence of leaks, resulted in an error in measured permeation rates of approximately ±10% of absolute values (note that error bars are only shown in the data presented when we are concerned with differences in permeation rates).

Oxygen permeation experiments

During permeation experiments, the gas-phase oxygen supplied to the oxygen side of the membrane was either 21% oxygen in helium or 21% oxygen in nitrogen, both ±5% accurate (the balance gas was chosen depending upon what form of in situ leak test, described later, was undertaken at the same time as collecting permeation data). On the other side of the membrane, the sweep side, 100% helium was used as the gas supply. The oxygen permeation rate, JO_2, was in general determined by the outlet mole fraction of oxygen appearing in the helium sweep gas, $[O_2]_{out}$ measured by GC, and using Eq. (2),

$$JO_2 = [O_2]_{out} F \frac{1}{V_m} \frac{1}{60} \quad (2)$$

where F is the flow rate of the helium sweep gas in ml (STP) min^{-1}, V_m is the volume to molar conversion of the oxygen content in the sweep (1 mole is equivalent to 22,400 ml at STP) and the final term converts the rate from minutes to seconds. Oxygen permeation data were recorded 15 min after changing the gas flow conditions and 30 min after each temperature change. For selected experiments, oxygen permeation was also determined from the oxygen consumption on the oxygen side. The two permeation rates were then compared as part of an oxygen balance.

Throughout this work, the side of the membrane, which is set to the higher oxygen partial pressure, is referred to as the oxygen side. The other side of the membrane is referred to as the sweep side. The sweep side contains a lower oxygen partial pressure; thus in principle, the oxygen permeation flow through the membrane is from the oxygen side to the sweep side. The oxygen side or the sweep side can be on the shell or lumen side. Under the highest temperature operating conditions, there was a significant drop in oxygen mole fraction between inlet and outlet on the oxygen side and a significant increase in mole fraction of oxygen or reaction products on the sweep side between inlet and outlet under both co-current and counter-current operation. Consequently, it is difficult to relate the flux to module gas phase compositions, and, instead in the figures, we relate flux to nominal inlet molar concentrations. For similar reasons, we do not report area-specific fluxes (except when comparing with the work of other researchers where we simply divide permeation rate by effective area to obtain an averaged flux) but prefer to report total transmembrane oxygen transport rates.

Leak tests and monitoring

Pre-operation leak tests were undertaken at oxygen permeation operating temperatures. In these experiments, pure nitrogen was used on one side of the membrane and pure helium on the other. In this simple leak test experiment, the mole fraction of nitrogen in the helium stream is quantified. The presence of this nitrogen is ascribed to gas phase transport through micro-cracks in the membrane. Oxygen in both the helium stream and the nitrogen stream is also measured. The presence of this oxygen is ascribed to gas phase transport through the module gas inlet and outlet seals and possible "degassing" of framework oxygen from the LSCF6428 lattice (the effect of oxygen leakage across the membrane is neglected as a first approximation due to the low partial pressure difference under these leak test conditions). It was found that the mole fraction of oxygen in the helium and nitrogen streams was always much less than that observed as a result of permeation in permeation experiments. The nitrogen leak as a function of temperature and flow rate is presented in Fig. 4. The leak rate appears to be fairly independent of temperature, and flow rate and is very much lower than the oxygen permeation rates that were observed in the permeation results presented later.

Furthermore, throughout the permeation and methane conversion studies, in situ leak tests were performed. The leak through the membrane to the sweep side (helium under permeation experiments and methane under methane oxidation experiments) was observed by using an oxygen–nitrogen gas mixture for the oxygen supply and measuring the nitrogen mole fraction at the outlet of the sweep side. Atmospheric leaks into the reactor were monitored by using an oxygen–helium mixture on the oxygen side and measuring nitrogen at both the outlet of the sweep side and the oxygen side. Detection of nitrogen was used as the indicator for sealant failure. The transmembrane oxygen transport rate is adjusted by subtracting the rate of oxygen leakage, calculated as 0.27 (1:3.7, oxygen to nitrogen ratio) multiplied by the nitrogen leak rate into the sweep side of the system. It should be noted that this oxygen leak rate was monitored over the entire course of experiments and, as expected, was seen to increase with time. However, with a fresh module the value of the oxygen leak rate was typically two orders of magnitude lower than the transmembrane oxygen transport rate.

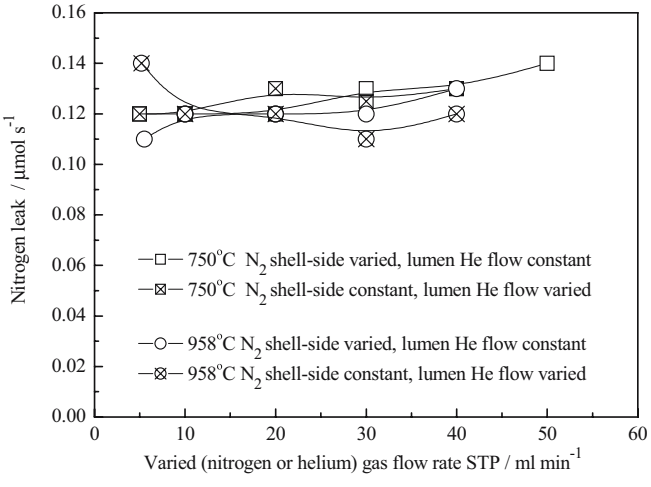

Fig. 4 Nitrogen leak from the shell side through the hollow fibre membranes at 750 and 958°C in co-current operation with either nitrogen or helium fixed at 50 ml min^{-1}, and the other gas varied from 5 to 50 ml min^{-1}

Methane oxidation experiments

During methane oxidation experiments, methane was supplied to the sweep side of the membrane. The methane supply was 5% methane in helium (accurate to ±5%) that was diluted with helium to give a shell-side, reactor-inlet methane concentration of 2.2% for these experiments. Again, gas-phase oxygen supplied to the oxygen side of the membrane was either 21% oxygen in helium or 21% oxygen in nitrogen. At the beginning of each experiment, data were collected at 15-min intervals over the first 2 to 4 h, then at 30-min intervals for 5 h and finally at 60-min intervals until the end of the experiment. The oxygen permeation during these experiments was estimated using the oxygen content of the oxygen-containing species produced during the reaction, i.e. unreacted oxygen permeate, carbon dioxide, carbon monoxide and water.

$$JO_2 = \left([O_2]_{out} + [CO_2]_{out} + 1/2\,[CO]_{out} + 1/2\,[H_2O]_{out}\right) F \frac{1}{V_m}\frac{1}{60} \quad (3)$$

where F and V_m are as defined previously. The other gas-phase product was hydrogen; no C_2 products were observed. Outlet-water mole fraction was not measured directly but calculated from a hydrogen balance on the sweep side that assumed there was no hydrogen accumulation in the module.

Results and discussion

Characterisation

Before use, each LSCF6428 hollow fibre was tested for gas tightness, and samples of the hollow fibre were ground for powder XRD, which revealed that the membranes employed in this work had retained the original perovskite structure but with broader reflections compared to those of the unused powder, which indicated a lowering of the crystal symmetry (powder pattern not shown). Typical SEM characterisation data are shown in Fig. 5.

The hollow fibres have an outer diameter of ca 1.5 mm and an internal diameter of ca 1 mm. Specimens typically do not have a regular circular cross-section but become distorted after sintering, giving rise to varying wall thickness (Fig. 5a). The insert of Fig. 5a shows the wall

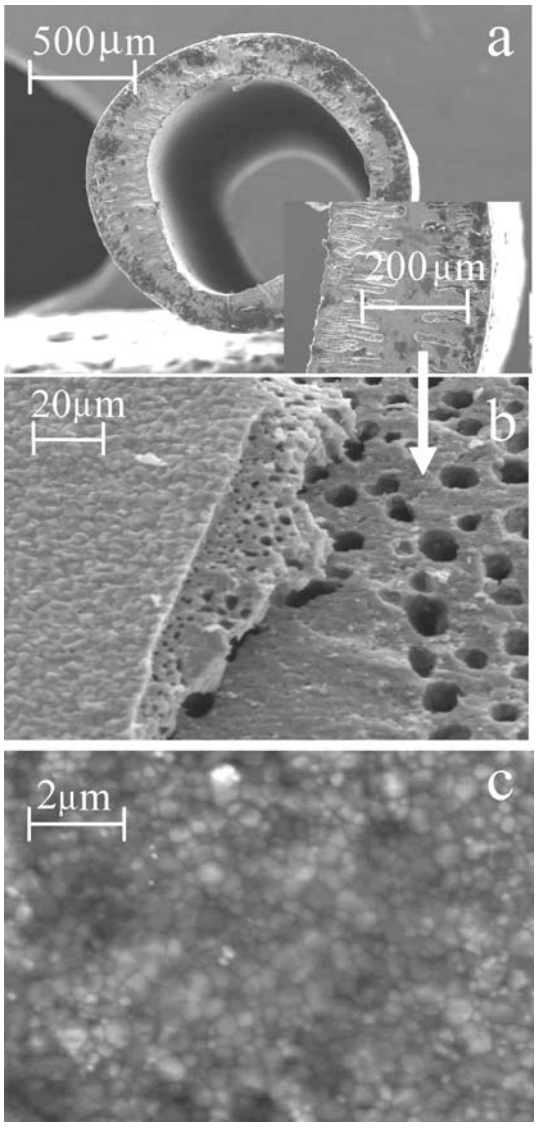

Fig. 5 **a** SEM image of the cross-section of a typical hollow fibre used in this work **b** SEM image of a hollow fibre membrane outer surface revealing the skin layer and interior honeycombed layer **c** SEM image of a hollow fibre membrane outer wall surface

cross-section more closely. The thickness is around 200 µm, and elongated, fingerlike cavities can be seen below the surface in profile. The cavities shown in Fig. 5a can be seen from a different view point in Fig. 5b, where the outer surface of the hollow fibres is revealed to be a "skin" of LSCF6428 membrane covering an inner honeycombed section produced by the cavities. The entrances to these cavities have diameters in the 5- to 10-µm range. Fabrication without this outer layer, or removal of the outer layer, would allow access to the cavities, resulting in higher membrane surface area that would potentially provide a good surface for catalyst incorporation (such modification of the fabrication process was not explored here). The outer membrane skin showed a continuous connection of grains, with sizes below 2 µm in diameter (Fig. 5c).

Oxygen permeation studies

For the purposes of this study, we first investigate oxygen permeation rates, dependent on which side of the membrane (lumen vs shell) the oxygen supply and helium sweep gas are used, the flow rates of these gases and temperature. Figures 6 and 7 show the dependence of the oxygen permeation rate on flow rate when 21% of oxygen (in either nitrogen or helium) is supplied to one side of the membrane with pure helium on the other.

The two temperatures used for this experiment cover the range for oxygen transport studies commonly investigated. In addition, both co-current and counter-current gas flow operation were employed. In this experiment, either the pure helium sweep or the 21% oxygen in nitrogen oxygen-side supply flow rate was fixed at 50 ml min^{-1}, and the other gas flow rate varied from 2 to 85 ml min^{-1}. A background leak rate of oxygen from the nitrogen into the

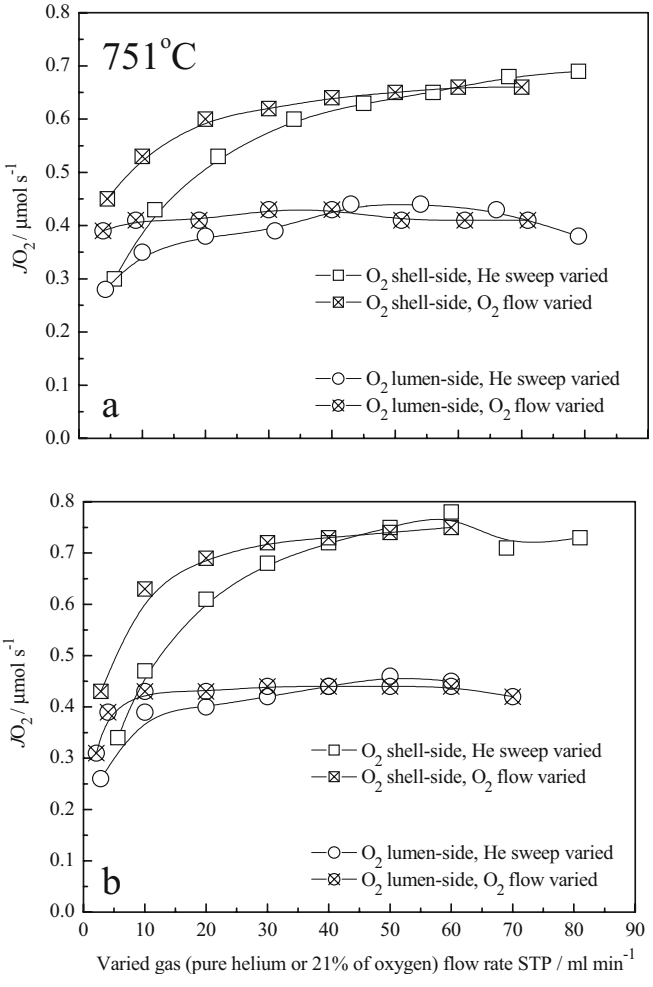

Fig. 6 Solid state oxygen permeation trends recorded at 751°C using oxygen at 21% in nitrogen or helium as the oxygen supply and 100% helium as sweep gas **a** co-current operation and **b** counter-current operation. The *circles* represent the oxygen supplied on the lumen side and the *squares* represent oxygen supplied on the shell side. *Open symbols* show the oxygen permeation as the helium sweep is varied and the *crossed symbols* as the oxygen flow is varied. The constant gas flow is 50 ml min^{-1}

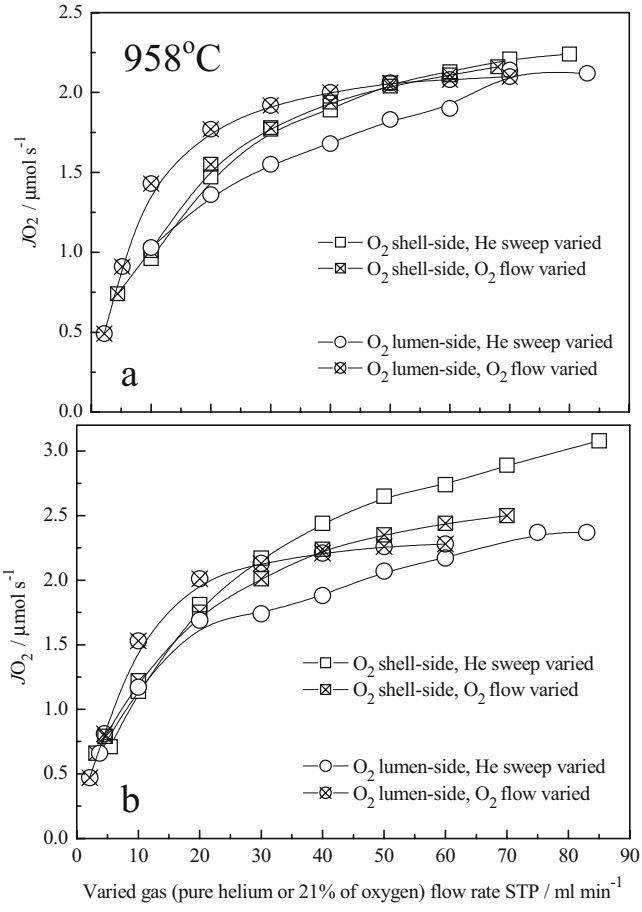

Fig. 7 Solid state oxygen permeation trends recorded at 958°C using oxygen at 21% in nitrogen or helium as the oxygen supply and pure helium as sweep gas **a** co-current operation and **b** counter-current operation. The *circles* represent the oxygen supplied on the lumen side and the *squares* represent oxygen supplied on the shell side. *Open symbols* show the oxygen permeation as the helium sweep is varied and the *crossed symbols* as the oxygen flow is varied. The constant gas flow is 50 ml min^{-1}

sweep side from both the atmosphere and the oxygen side was measured in situ and found to be ca 0.03 µmol O_2 s^{-1}. At 751°C, there are two clear oxygen permeation regimes observed for both co-current (Fig. 6a) and counter-current operations (Fig. 6b). The highest permeation rate at this temperature is obtained when the oxygen is supplied to the shell side for both cases. The ratio of the outer to inner radii of the hollow fibres is ca 1.4. This is reasonably close to the ratio of the oxygen permeation values with oxygen on the shell side vs the lumen side under co-current operation (1.5) and counter-current operation (1.75). This may be indicative of a rate-determining step being associated with processes at the oxygen-exposed surface, possibly involving oxygen reduction to form oxygen ions. In addition, it can be seen that with one flow rate below ca 40 ml min^{-1}, the permeation rate is dependent upon the value of this flow rate. This is consistent with mass transfer resistances under such conditions. At 751°C, the highest oxygen permeation rate resulted in a decrease in oxygen mole fraction on the oxygen side from 21 to 19%, showing that the driving force for oxygen permeation (in terms of mole fraction or partial pressure) was not a strong function of position in the reactor.

At 958°C (Fig. 7), the behaviour is markedly different to that at 751°C. We generally observe significantly higher rates of permeation. At this temperature, there is a sharp increase in permeation rates, as one flow rate is increased to ca 30 ml min^{-1} followed by a gentler increase up to ca 85 ml min^{-1}. The oxygen permeation rate is not a strong function of which gas is supplied to the higher area shell side of the module, implying that surface processes are not rate-determining. The data are consistent with mass transfer limitations being important over, what is now, a broader range of flow rates. Mass transfer would be expected to be more significant at higher temperatures, as the chemical processes associated with oxygen permeation are activated processes. At 958°C, the highest oxygen permeation rate resulted in a decrease in oxygen mole fraction on the oxygen side from 21 to 15%, showing that the driving force for oxygen permeation (in terms of mole fraction or partial pressure) was a stronger function of position in the reactor at these temperatures. These modest oxygen conversions are consistent with the oxygen permeation rate being essentially independent of mode of operation, i.e. counter-current vs co-current.

The highest permeation achieved in these experiments was 3.15 µmol s^{-1} (equivalent to 4.23 ml min^{-1}) at 958°C under counter-current operation, and the lowest was 0.26 µmol s^{-1} (equivalent to 0.35 ml min^{-1}) at 751°C under counter-current operation. Estimating fluxes gives approximate values of 0.31 (0.42 ml cm^{-2} min^{-1}) and 0.03 µmol O_2 cm^{-2} s^{-1} (0.04 ml cm^{-2} min^{-1}). As permeation rates are not a strong function of the mode of operation under these conditions, henceforward, we confine ourselves to co-current operation. Furthermore, for the remaining permeation experiments, oxygen was supplied to the shell side with the sweep side therefore being in the lumen.

The effect of temperature on the rate of oxygen consumption from the oxygen side and the rate of oxygen release into the sweep side, for a constant set of gas flow conditions under co-current operation (to address a crude form of oxygen balance), is presented in Fig. 8. The experiment was initiated at 958°C with subsequent data recorded in decreasing 20 or 30°C steps down to 543°C. Each pair of data points was recorded 30 min after the desired temperature was reached, except for the pair of data points at 626°C, which was recorded 12 h after the temperature was reached.

As shown in Fig. 8, we observe that both oxygen permeation rates have an almost linear dependence on temperature above 750°C. We note that at module centre temperatures below 750°C, the oxygen balance does not close, and the oxygen permeation rate measured by consumption is greater than the oxygen permeation rate measured by release in the helium sweep. This behaviour may have its origins in structural order–disorder phase changes within the LSCF6428 lattice due to the take up of oxygen with resultant oxygen stoichiometry changes.

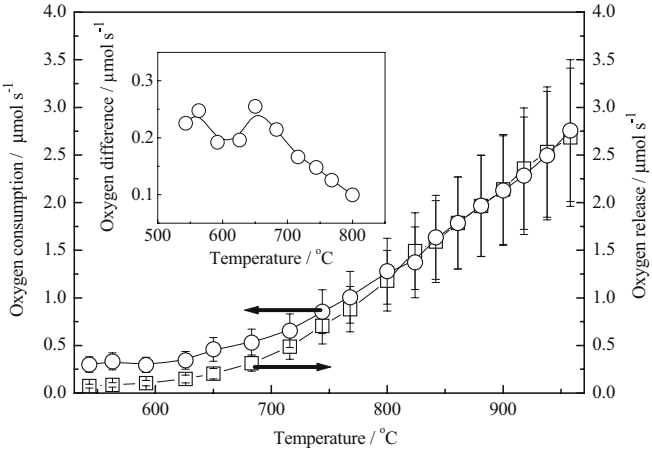

Fig. 8 Comparison between oxygen consumption on the shell side and oxygen release on the lumen side compared to the oxygen permeation in μmol s^{-1} as a function of temperature with oxygen-nitrogen gas supplied at 50 ml min^{-1} and fixed lumen side helium sweep of 50 ml min^{-1}

Further analysis is complex due to the temperature profile along the membranes, but it should be remembered that a phase transition at, e.g., 800°C could also occur at higher module centre temperatures because of this temperature profile.

After reaching 543°C, a limited number of further permeation data points were taken to check for hysteresis (not shown). A small decrease of, at the most, 7% compared to the original permeation values was observed and was not considered to be significant within the uncertainty associated with the permeation rates.

It is interesting to note that even at the "cold" operating temperature of 543°C, the thin membrane wall and the high surface area of the six hollow fibres allow us to observe a real oxygen permeation rate (based upon release into the sweep side) of 0.07 μmol s^{-1} (note that the permeation rate, based upon oxygen consumption from the oxygen side, was much greater than this value under these conditions). This is approximately double the value of the background oxygen leakage into the module from the atmosphere.

The oxygen permeation observed in this work is compared to data taken from other systems operating at a pressure of 1 atm (see Table 1). The data were obtained by inspection of graphical figures when values were not stated in the cited work. The table shows minimum and maximum oxygen permeation fluxes for LSCF6428 in disc and tubular forms compared to that for hollow fibre form. Also shown for comparison are oxygen permeation data from two other materials, $Ba_{0.5}Sr_{0.5}Co_{0.8}Fe_{0.2}O_{3-\delta}$ and $BaSr_xCo_yFe_zO_{3-\delta}$ in hollow fibre form, which have been reported to exhibit much higher oxygen fluxes than that obtained for LSCF6428.

The importance of membrane thickness is not apparent. It appears that maximum fluxes may be somewhat higher in the case of the hollow fibres. However, there is some significant uncertainty in how much active surface area is available in the hollow fibre systems. Consequently, the evidence that hollow fibres are providing a greater oxygen flux is weak. However, it is interesting to note that in this

Table 1 Comparison of oxygen permeation performance of hollow fibre membrane LSCF6428 with other geometries and membrane materials

Membrane material	Membrane form	Thickness (mm)	Temperature (°C)	Flux jO_2[a]		Atmospheres used[b]	Reference
				ml cm^{-2} min^{-1}	μmol $cm^{-2}s^{-1}$	low pO_2 | high pO_2	
$La_{0.6}Sr_{0.4}Co_{0.2}Fe_{0.8}O_{3-\delta}$	Disc	2.3–3.1	775–925	0.1–0.45	0.07–0.3	N_2 | 1 atm O_2	[10]
$La_{0.6}Sr_{0.4}Co_{0.2}Fe_{0.8}O_{3-\delta}$	Disc	1.68–3.99	75–950	0.02–0.24	0.01–0.17	N_2 / 0.001 atm O_2 | 1 atm O_2	[11]
$La_{0.6}Sr_{0.4}Co_{0.2}Fe_{0.8}O_{3-\delta}$	Disc	0.96	800 and 1,000	0.04	0.03	He / 0.001 atm O_2 | Air	[12]
$La_{0.6}Sr_{0.4}Co_{0.2}Fe_{0.8}O_{3-\delta}$	Tubular	1.5	900	0.13	0.1	He / 0.001 atm O_2 | Air	[18]
LSCF6428 asymmetric membrane	Disc	1–2	600–800	0.1–0.18	0.07–0.13	He | Air	[19]
$La_{0.6}Sr_{0.4}Co_{0.2}Fe_{0.8}O_{3-\delta}$	Disc	1.43, 1.53	800–1,000	0.04–0.22	0.03–0.17	Ar | Air	[20]
$La_{0.6}Sr_{0.4}Co_{0.2}Fe_{0.8}O_{3-\delta}$	Hollow fibre	0.2[c]	543–958	0.09–0.42[d]	0.07–0.3[d]	He | Air	This work
$La_{0.6}Sr_{0.4}Co_{0.2}Fe_{0.8}O_{3-\delta}$	Hollow fibre	0.2[c]	858	0.26–0.8[d]	0.2–0.6[d]	0.022 atm CH_4 | Air	This work[e]
$La_{0.6}Sr_{0.4}Co_{0.2}Fe_{0.8}O_{3-\delta}$	Hollow fibre	0.3[c]	800–900	0.1–1.2	0.07–0.9	Ar | Air	[14]
$La_{0.6}Sr_{0.4}Co_{0.2}Fe_{0.8}O_{3-\delta}$	Hollow fibre	0.2[c]	700–900	0.1–0.8	0.07–0.55	Ar | Air	[15]
$Ba_{0.5}Sr_{0.5}Co_{0.8}Fe_{0.2}O_{3-\delta}$	Hollow fibre	0.2[c]	700–950	0.69–5	0.51–3.72	He | Air	[21]
$BaZr_xCo_yFe_zO_{3-\delta}$[f]	Hollow fibre	0.18	800–900	4–7.6	2.98–5.65	He | Air	[22]

[a]STP presumed where not stated
[b]Low oxygen content side value quoted where stated
[c]Approximate thickness
[d]From estimated active membrane area (ca 10 cm^{-2})
[e]Includes periodic surge in permeation
[f]Stoichiometry not given

work, there is a measurable oxygen flux at a much lower temperature than in any of the other work. This may be a result of the increased surface area for oxygen reduction and the decrease in effective membrane thickness. Such evidence is a much clearer demonstration that the hollow fibres may be able to deliver greater fluxes under appropriate conditions.

Methane oxidation

Oxygen permeation using methane–helium as sweep

The methane oxidation studies were undertaken using the same module employed for the above oxygen permeation studies. Initial investigations (not shown) revealed that the rate of methane oxidation was significantly higher for any given set of reaction conditions, when the methane was supplied on the shell side and oxygen through the hollow fibre lumen side. The data presented in this section were obtained using this configuration in co-current operation. The LSCF6428 hollow fibre membranes were not catalytically modified. The studies were all performed at a nominal 860°C (module centre temperature) and the products (with the exception of water), unreacted oxygen permeate and unreacted methane were monitored with time. The only controlled variable in these experiments was the rate of the gas-phase oxygen supply through the lumen side, with the methane–helium mixture on the shell side acting as the sweep gas at a fixed flow rate and with fixed inlet composition. The lowest temperature at which significant methane conversion was observed was 860°C. No C_2 products were observed. During methane oxidation experiments, an initial oxygen leak of 0.04 μmol s^{-1} was observed on the shell side, increasing to 0.07 μmol s^{-1} towards the end of the study. The initial leak rate, in the case of the permeation experiments (of 0.03 μmol s^{-1}), and the increase to 0.07 μmol s^{-1} may be indicative of deterioration of the membranes under reaction conditions coupled with a small amount of sealant failure due to aging.

Figure 9 shows the total oxygen permeate during methane oxidation performed using 21% oxygen in nitrogen at the oxygen side inlet and 2.2% methane in helium at the sweep side inlet at a nominal operating temperature of 858°C for four different oxygen–nitrogen inlet flow rates.

The oxygen–nitrogen inlet flow rates used were 10 ml min^{-1} (1.55 μmol s^{-1} of oxygen), 20 ml min^{-1} (3.10 μmol s^{-1} of oxygen), 30 ml min^{-1} (4.66 μmol s^{-1} of oxygen) and 40 ml min^{-1} (6.21 μmol s^{-1} of oxygen). The methane–helium inlet flow rate was fixed at 50 ml min^{-1} (0.81 μmol s^{-1} of methane) on the shell side. In the absence of the membrane barrier, these flow rates would give an oxygen-to-methane inlet molar feed ratio of 1.9, 3.8, 5.7 and 7.6. The oxygen permeation generally increases over time after an initial drop. Periodic increases in the oxygen permeation rate were observed. These increases influenced the methane conversion and product distribution during the methane oxidation reaction. However, we can see that the

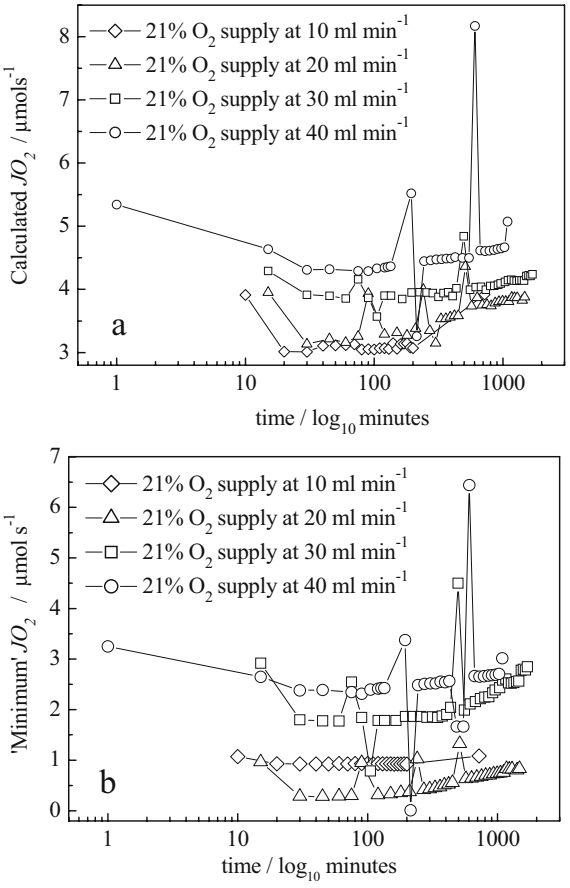

Fig. 9 Oxygen permeation during methane combustion at 858°C in co-current operation with 2.2% of methane in helium supplied at 50 ml min^{-1} on the shell side and 21% oxygen in nitrogen supplied on the lumen side at 10, 20, 30 and 40 ml min^{-1} **a** calculated from unreacted oxygen permeate, oxygen containing species and oxygen from calculated water content and **b** calculated only from unreacted oxygen permeate and detected oxygen-containing species

calculated oxygen permeation rate is, in many cases, greater than the total oxygen flow supplied to the module. As the module operates over a significant period of time (of the order of 24 h) with no sign of membrane failure and at these fluxes, we would expect oxygen to be rapidly depleted from the lattice. We must question the method for calculating the oxygen permeation rate under reaction conditions. We recall that calculation of this permeation rate was based upon the assumption that there was no hydrogen accumulation within the system. However, if carbon deposition proceeds, it is likely that hydrogen associated with the carbonaceous deposit will accumulate within the module. As water was not measured in the sweep side outlet, we now determine, as an approximation, a "minimum" oxygen permeation rate using the following equation,

$$\mathrm{JO_2} = \left([\mathrm{O_2}]_{\mathrm{out}} + [\mathrm{CO_2}]_{\mathrm{out}} + 1/2[\mathrm{CO}]_{\mathrm{out}}\right) F \frac{1}{V_m} \frac{1}{60} \qquad (4)$$

where, essentially, all hydrogen not specifically observed as hydrogen in the outlet is assumed to have remained in the reactor. Figure 9b shows this revised minimum oxygen permeation rate as a function of time. It is interesting to note that the pulses in these sweep-side-determined oxygen permeation rates correspond very closely with the rate of oxygen supply on the oxygen side. This implies that during an oxygen pulse, there is closure of full utilisation of oxygen from the oxygen side. This tentatively supports our assumption that there is very little water production on the sweep side.

The total oxygen permeation rate under reaction conditions (see Fig. 9, ca 2.5–3 μmol s^{-1} at 858°C, 40 ml min^{-1} oxygen side flow rate) was found to be more than the oxygen permeation rate obtained in the oxygen permeation study (see Fig. 8, ca 1.7 μmol s^{-1} at 861°C, 50 ml min^{-1} oxygen side flow rate) using helium as the sweep. As a result of the increased effective oxygen chemical potential difference under reaction conditions, one would expect the permeation rate to be higher.

Product yields and product distribution

Figure 10a–d shows the percentage carbon yields of the gas-phase carbon-containing species; carbon monoxide, carbon dioxide and methane, along with the conversion of methane (this being one minus the methane yield).

It is evident that the flow rate of the oxygen on the oxygen side has a strong effect on product yields on the shell side. At the oxygen inlet flow rate of 10 ml min^{-1}, the conversion of methane on the sweep side is around 40% for most of the duration of this experiment. Interestingly, at the beginning of the experiment, the conversion is higher, but after 20 min, falls to this lower stable value for a period of almost 12 h. At the end of the 12-h period, the conversion increases abruptly. The yields of individual products do not vary greatly when the conversion is around 40%. It can be observed that the yields of the carbon-containing species do not add up to unity. Figure 11 shows a plot of the yield of the unaccounted for carbon, which is likely to have been deposited somewhere within the module.

As the oxygen inlet flow rate is increased to 20 ml min^{-1}, the oxygen permeation rate increases along with the methane conversion. We note that the product distribution is generally time-dependent. Periodic fluctuations were observed in the oxygen outlet mole fraction from the sweep side (i.e. reaction side). The oxygen outlet mole fraction exhibited four reversible pulsed increases over 24 h. The first fluctuation was observed at the beginning of the experiment, with the second, third and fourth occurring ca 80, 150 and 270 min late, respectively. The fluctuations have an increasing period and coincided with the methane conversion reaching 100% and increased carbon dioxide production, with a corresponding decrease in carbon monoxide yield. The oxygen permeation rate was found to gradually increase over the 24-h experimental observation period.

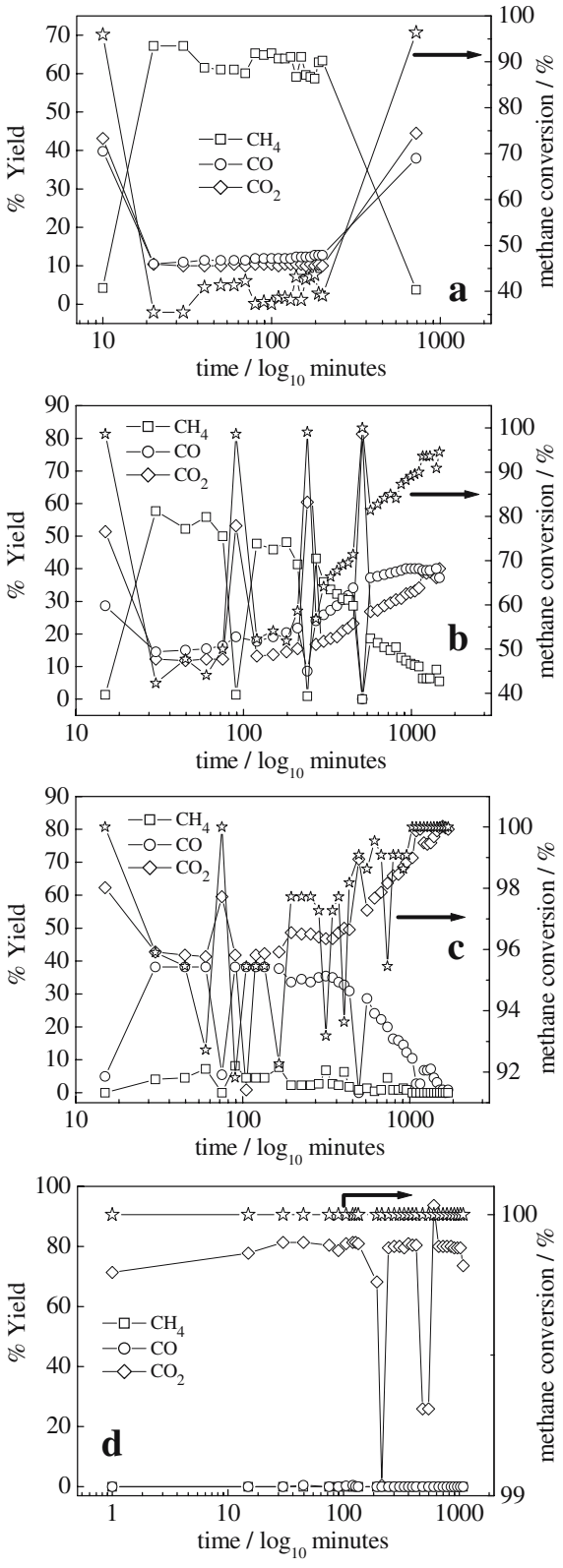

Fig. 10 Plots of the percent yield of gaseous carbon-containing species during methane oxidation over time at 858°C with 2.2% methane in helium on the shell side and 21% oxygen in nitrogen supplied through the lumen side at **a** 10 ml min^{-1}, **b** 20 ml min^{-1}, **c** 30 ml min^{-1} and **d** 40 ml min^{-1} in co-current operation. The *star* symbol shows the methane conversion, which is indicated on the *right-hand axis*

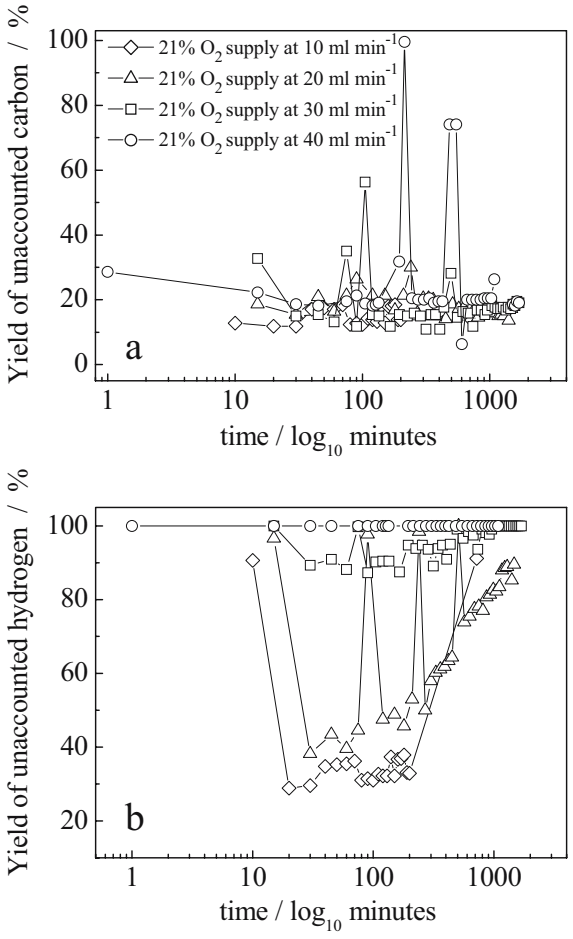

Fig. 11 Plots of the unaccounted carbon **a** and unaccounted hydrogen **b** percent yield during methane oxidation over time at 858°C with 2.2% methane in helium on the shell side and 21% oxygen in nitrogen supplied through the lumen side at, 10, 20, 30 and 40 ml min^{-1} in co-current operation

At an oxygen supply of 30 ml min^{-1} (Fig. 10c), the oxygen permeation fluctuations are less frequent but more pronounced. The methane conversion is close to 100% from the beginning of the analysis, with the main detected product being carbon dioxide. A gradual decline in carbon monoxide yield and an increased carbon dioxide yield after ca 10 h became apparent.

When the oxygen is supplied at 40 ml min^{-1} (Fig. 10d), the conversion of methane is complete and, therefore, constant over the 18-h period of observation. Only trace amounts of carbon monoxide were observed, and carbon dioxide was the main carbon-containing product. Again, there were fluctuations in the oxygen permeation rate, which became particularly large. These fluctuations in oxygen permeation rate were associated with very low carbon yields of gas-phase species and increased oxygen mole fraction in the sweep-side outlet. It must be remembered that gas-phase composition data are discrete data and not continuous. Even though no significant changes in the outlet flow rate from the sweep side were noted, it is conceivable that during an oxygen pulse, there could be a dilution effect leading to lower apparent (with flow rate changes unaccounted for) carbon yields.

As previously mentioned, Fig. 11 shows the yield of carbon deposited in the module. To obtain this data, carbon balances were performed. The yield of the unaccounted for carbon, Y_C, was determined from,

$$Y_C = \frac{[CH_4]_{in} - [CH_4]_{out} - [CO]_{out} - [CO_2]_{out}}{[CH_4]_{in}} = \frac{[C]}{[CH_4]_{in}} \quad (5)$$

Between ca 10 and 25% of the carbon fed to the reactor appears to form carbon deposits.

Figure 11 also shows the results from performing hydrogen balances. The yield of unaccounted for hydrogen is the yield of hydrogen in any deposits in the module plus the yield of water,

$$Y_H + Y_{H_2O} = \frac{[CH_4]_{in} - [CH_4]_{out} - 1/2[H_2]_{out}}{[CH_4]_{in}} = \frac{1/4[H] + 1/2[H_2O]_{out}}{[CH_4]_{in}} \quad (6)$$

The yield of unaccounted for hydrogen is generally much greater than that of carbon. As we would not expect polymeric carbon deposits to have a hydrogen to carbon ratio of more than two (a hydrogen to carbon yield ratio of one half), there must be very significant water production under many conditions, and oxygen permeation fluxes will be somewhat larger than those reported in this contribution.

It is possible that the carbonaceous deposits are acting as a barrier to oxygen permeation and that the oxygen permeation observed is lower than the maximum that the membranes can deliver. A further complication is the possible formation of new phases as a result of the LSCF6428 perovskite undergoing reaction. This would also result in reduced oxygen permeation. However, the 2.2% of methane used in this study is not severely reducing (in studies of the type described here even pure methane is frequently used).

Post methane oxidation oxygen permeation study

Following the methane conversion experiments, the module was cooled to room temperature. A repeat oxygen permeation study was undertaken to see if the presence of methane and the products produced by its conversion had affected the oxygen permeation behaviour compared to the first observations shown in Figs. 6, 7 and 8. The same experimental conditions were employed, i.e. co-current operation with the oxygen supply and the pure helium sweep both at flow rates of 50 ml min^{-1}. Note that the oxygen is now supplied to what was the sweep side (methane side) under methane oxidation reaction conditions.

It was found that over 16 h of operation, the oxygen permeation rates at 750 and 850°C were around half of the values originally recorded at these temperatures before exposure to methane (data not shown). The module was then heated to 958°C and both the shell- and lumen-side outlet oxygen mole fractions recorded simultaneously over 115 h. Figure 12 shows the rate of oxygen release into the sweep side and the rate of oxygen consumption at the oxygen side. The difference between these two rates should be due to oxidation of carbonaceous deposits and/or any change in membrane stoichiometry.

The oxygen consumption rate on the oxygen side decreased steadily over a period of 95 h, whereupon a sudden increase occurred that stabilised within 60 min after a small overshoot. A simple explanation of this decline is that the oxygen being consumed on the oxygen side, in excess of that accounted for as oxygen released on the sweep side, is oxidising carbonaceous deposits formed during the methane oxidation studies on the hollow fibre surfaces. At 750 and 850°C, this process was slow and the coke remained on the surface, hindering oxygen permeation. When switching to 958°C, enough of the carbonaceous deposits were oxidised, presumably to carbon dioxide (no gas analysis for carbon oxides was performed), to allow the permeation rate to attain its original value. The sudden increase in rate of oxygen consumption after 95 h is surprising. This could be due to a more stable carbonaceous deposit finally being removed, or it could be due to change in membrane stoichiometry. The rate of oxygen consumption was not followed over longer time scales to shed light on these hypotheses.

Initially, the oxygen rate of release (ca 2.0 μmol s^{-1}) is lower than the oxygen permeation rate obtained before the methane conversion studies (originally ca 2.5 μmol s^{-1} was obtained, as shown in Fig. 7). After ca 30 h, the rate of oxygen release increases to ca 2.5 μmol s^{-1}, close to this original value of the permeation rate. A possible explanation for the gradual increase in the rate of oxygen release is that an induction period is required for the LSCF6428 membrane to establish the steady-state oxygen vacancy distribution throughout the membrane [23]. When this is established, a steady oxygen solid-state flux is achieved. In LSCF6428 disc membranes of thickness 1.57 and 1.88 mm, this period has been found to be 15 and 22 h long, respectively [23].

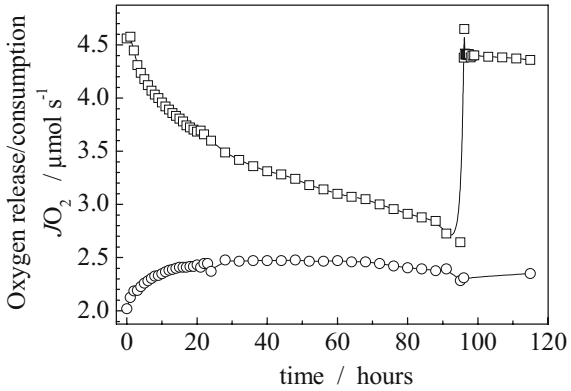

Fig. 12 Post methane oxidation permeation study recorded at 958°C using oxygen at 21% in nitrogen as the oxygen supply at 50 ml min^{-1} on the shell side and pure helium as sweep gas at 50 ml min^{-1} on the lumen side in co-current operation. The *circles* represent the oxygen release and the *squares* represent the oxygen consumption

Similar fluctuations to those observed in the rate of oxygen release at ca 30 and 90 h have been observed by Xu et al. [24] in studies using a tubular LSCF6428 membrane. They ascribed the fluctuations to traces of sulphur found on the membrane surfaces in the form of $SrSO_4$ and $CoSO_4$. The source of the sulphur was found to be the atmosphere and the helium gas supply used in their studies. The irregular rate of oxygen release disappeared after the removal of the sulphur contamination. The rate was then stable for 80 h. It is possible that surface contamination is also important in the work presented here. This would of course have an impact on measured rates of oxygen permeation.

Conclusions

A reactor module consisting of six gas-tight hollow fibre membranes made of the mixed ionic-electronic conducting perovskite $La_{0.6}Sr_{0.4}Co_{0.2}Fe_{0.8}O_{3-\delta}$ has been tested for oxygen permeation and stability during methane oxidation in the temperature range of 540 to 960°C. Rigorous leak testing was undertaken and it was demonstrated that the module could be adequately sealed. Oxygen permeation fluxes were similar to those reported by previous workers. At higher temperatures of operation, it appeared that mass transfer limited the oxygen flux, as this flux was dependent upon the flow rates on either side of the membrane. In this way, reactant flow rates could be used to manipulate the transmembrane oxygen flux. It was found that the product distribution on the methane side was dependent upon this flux, with carbon monoxide and hydrogen production being favoured at low fluxes and carbon dioxide and water production being favoured at higher fluxes. Furthermore, at low oxygen flow rates, periodic increases in the transmembrane oxygen flux were observed. The cause of this behaviour is unclear but may be as a result of phase/stoichiometric changes associated with the membrane material. Carbonaceous deposits are clearly formed on the membrane surface when exposed to methane. These deposits appear to inhibit permeation rates with rates returning to original values when the deposits are removed by reaction with oxygen.

Acknowledgements This work was funded by the EPSRC through grant number GR/S12197. The authors would like to thank Dr. Kang Li of Imperial College for supplying the hollow fibres used in this study.

References

1. Arakawa H (2001) Chem Rev 101:953
2. Yantovski E, Gorski J, Smyth B, ten Elshof J (2004) Energy 29:2077
3. Peña MA, Fierro JLG (2001) Chem Rev 101:1981
4. Smyth DM (2000) Solid State Ion 129:5
5. Tao S, Irvine TS (2002) Solid State Ion 154:659
6. Catalysis Today (1990) 8: all references therein
7. Mineshige A, Izutsu J, Nakamura M, Nigaki K, Abe J, Kobune M, Fujii S, Yazawa (2005) Solid State Ion 176:1145
8. Thursfield A, Metcalfe IS (2004) J Mater Chem 14:2475
9. Teraoka Y, Zhang HM, Okamoto K, Yamazoe N (1988) Mater Res Bull 23:51
10. Stevenson JW, Armstrong TR, Carneim RD, Pederson LR, Weber WJ (1996) J Electrochem Soc 143:2722
11. Xu JS, Thomson WJ (1999) Chem Eng Sci 54:3839
12. Lane JA, Benson SJ, Waller D, Kilner JA (1999) Solid State Ion 121:201
13. Li S, Jin W, Huang P, Xu N, Shi J, Lin YS (2000) J Membr Sci 166:51
14. Tan X, Liu Y, Li K (2005) AIChE J 51:1991
15. Tan X, Lui Y, Li K (2005) Ind Eng Chem Res 44:61
16. de Jong J, Benes NE, Koops GH, Wessling M (2004) J Membr Sci 239:265
17. Nijdam W, de Jong J, van Rujn CJM, Visser T, Versteeg L, Kapantaidakis G, Koops GH, Wessling M (2005) J Membr Sci 256:209
18. Li S, Qi H, Xu N, Shi J (1999) Ind Eng Chem Res 38:5028
19. Jin W, Li S, Huang P, Xu N, Shi J (2001) J Membr Sci 185:237
20. Diethelm S, Van herle J (2004) J Eur Ceram Soc 24:1319
21. Liu S, Gavalas GR (2004) J Membr Sci 246:103
22. Schiestel T, Kilgus M, Peter S, Caspary KJ, Wang H, Caro J (2005) J Membr Sci 258:1
23. Xu SJ, Thomson WJ (1998) Ind Eng Chem Res 37:1290
24. Xu N, Li S, Jin W, Shi J, Lin YS (1999) AIChE J 45:2519